frontiers | Frontiers in Physics

TYPE Original Research
PUBLISHED 27 July 2023
DOI 10.3389/fphy.2023.1227013

OPEN ACCESS

EDITED BY
Li Li,
Harbin Institute of Technology, China

REVIEWED BY
Giuseppe Brunetti,
Politecnico di Bari, Italy
Yongzheng Wen,
Tsinghua University, China

*CORRESPONDENCE
Ruoxing Wang,
wangruoxing@hrbeu.edu.cn

RECEIVED 22 May 2023
ACCEPTED 17 July 2023
PUBLISHED 27 July 2023

CITATION
Ren Z, Wang W, Zhao Y, Chang S, Ren G, Li S and Wang R (2023), A switchable terahertz metamaterial absorber between ultra-broadband and dual bands.
Front. Phys. 11:1227013.
doi: 10.3389/fphy.2023.1227013

A switchable terahertz metamaterial absorber between ultra-broadband and dual bands

Zhi Ren[1,2], Wanqing Wang[1,2], Yinghui Zhao[1,2], Siqi Chang[1,2], Guanhua Ren[1,2], Songtao Li[1,2] and Ruoxing Wang[1,2]*

[1]Department of Mathematics and Physics, North China Electric Power University, Baoding, China, [2]Heibei Key Laboratory of Physics and Energy Technology, North China Electric Power University, Baoding, China

Based on the phase change properties of vanadium dioxide (VO_2), we propose a terahertz metamaterial absorber that can be switched flexibly between ultra-broadband and dual bands. The absorber consists of a resonator array above a conductive ground layer separated with a dielectric spacer, which includes four square-loop VO_2 resonators and a crossed gold resonator in each unit cell. By changing the conductivity of VO_2 through thermal control, the absorber can achieve the switching between ultra-broadband absorption and dual-band absorption. Simulation results show that at high temperature, the absorber realizes more than 90% absorption bandwidth in the range of 3.98 to 9.06 THz, which can be elucidated by the wave-interference theory and impedance matching theory. At low temperature, up to 95% of the dual-band absorption occurs at 5.95 and 6.95 THz, which originates the dipole mode and nonlocal surface-Bloch mode of metal resonators. In addition, the absorber has the advantages of polarization-independence and wide-angle absorption. Compared with previous studies, our design can switch between two absorption modes and its absorption performance is greatly improved. The proposed absorber design scheme is expected to expand terahertz devices and enable a variety of applications in the terahertz range, such as modulation, sensing, stealth, and switching devices.

KEYWORDS

terahertz absorber, terahertz metamaterial, broadband absorption, dual-band absorption, switchable device

1 Introduction

Terahertz (THz) technology, usually in the frequency range from 0.1 to 10 THz, has a wide range of potential applications in the fields of sensing, imaging, and communication, due to its distinctive features such as high security, strong penetration, high temporal resolution and low background noise [1–5]. However, due to the lack of natural materials with strong responses to THz waves, the full development and utilization of THz technology are greatly limited. Over the past dozen years, through the design of artificial metamaterial, many novel phenomena have been brought from the visible to the microwave bands [6–9]. The size of metaatom can control the response frequency of metamaterial, which provides a tremendous impetus for the development of THz technology [10–13]. Various THz functional devices based on metamaterials have been proposed, such as THz filters [14–16], THz absorbers [17–19], and THz polarization converters [20–22]. Among these functional devices, THz metamaterial absorbers (TMAs), as one of the key elements in the

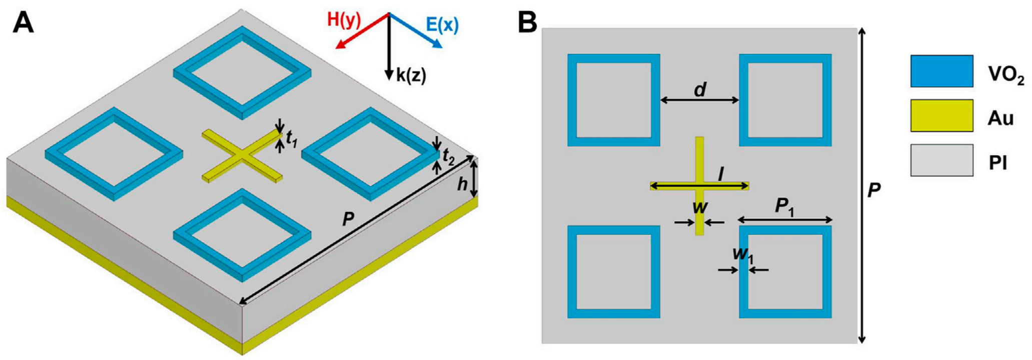

FIGURE 1
Schematic of the unit cell of the designed TMA under **(A)** the bird's eye view and **(B)** the top view.

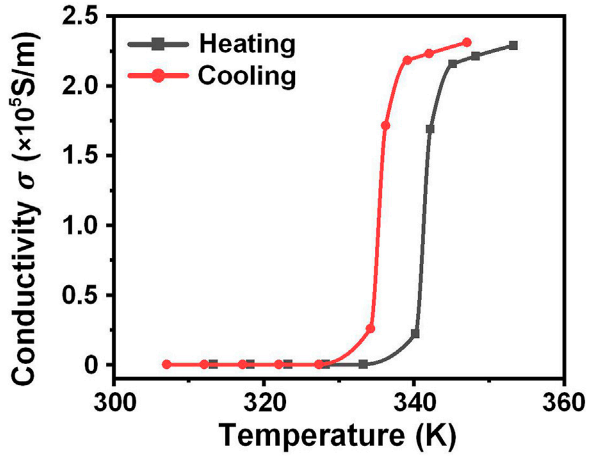

FIGURE 2
Conductivity of VO_2 with temperature.

THz detection system, have attracted much attention. With the advantages of strong absorption, thin thickness, and light mass, TMAs have potential applications in thermal emitters [23–25], photovoltaic cells [26–28], and stealth technologies [29–31].

The first demonstration of TMAs was achieved in 2008 [32]. Subsequently, various high-performance TMAs were proposed, including polarization-independent absorption [33, 34], multi-band absorption or broadband absorption [17, 35], high absorption under wide-angle incidence [36, 37], *etc.* Once the structural parameters are determined in these TMA schemes, the absorption performance of TMAs cannot be changed, greatly limiting their practical application. Recently, TMAs combining functional materials have been proposed, including semiconductors [17, 38], liquid crystals [39–41], graphene [42–44], and phase-change materials (PCMs) [45–47], achieving the tunability of TMAs, which meets the development needs of THz absorbers.

PCMs now are widely used for their fast and reversible switching between two atomic states, which can be triggered by heat, light or electricity. One of the most commonly used PCMs is vanadium dioxide (VO_2). It exhibits reversible phase transition behavior between the insulator phase and the metallic phase [48], which facilitates allowing smaller effective lengths and reducing power consumption compared to other commonly used PCMs [47, 49]. The phase transition from insulator to metal can be tuned by increasing the temperature, accompanied by a steady increase in the conductivity of VO_2 from 2×10^2 S/m to 2×10^5 S/m [50, 51]. Conversely, it can be tuned by cooling down, with the conductivity decreasing. Due to the flexibility of this electromagnetic characteristic modulation, some temperature-controlled tunable TMAs based on VO_2 have been proposed [52–55]. However, these TMA schemes focus more on broadband absorption performance at high temperatures, with little absorption effect at low temperatures, resulting in a single functionality. Functionally switchable TMAs can greatly expand their own available scenarios, in line with current development trends to address the scarcity of THz devices.

Recently, some VO_2-based TMAs integrated with PCMs or noble metals have been developed to achieve efficient absorption [43], beam steering [56], polarization conversion [21, 57], and electromagnetically induced transparency [58] at low temperatures. However, these designs increase the complexity of the structure or require simultaneous consideration of the phase transition conditions of other PCMs. Unlike previously reported studies, in this paper, we propose a TMA with simple structural design and polarization-independence that can be switched flexibly between ultra-broadband and dual bands by changing the conductivity of VO_2 through thermal control. The TMA consists of a resonator array above a conductive ground layer separated with a dielectric spacer, which includes four square-loop VO_2 resonators and a crossed gold (Au) resonator in each unit cell. When VO_2 is in the completely metallic state at high temperature, the TMA realizes more than 90% absorption bandwidth in the range of 3.98 to 9.06 THz which can be elucidated by the wave-interference theory and impedance matching theory. At low temperature where VO_2 is fully insulated, up to 95% of the dual-band absorption occurs at 5.95 and 6.95 THz, which originates the dipole mode and nonlocal surface-Bloch mode of metal resonators. Compared with previous studies, our design can switch between two absorption modes and its absorption

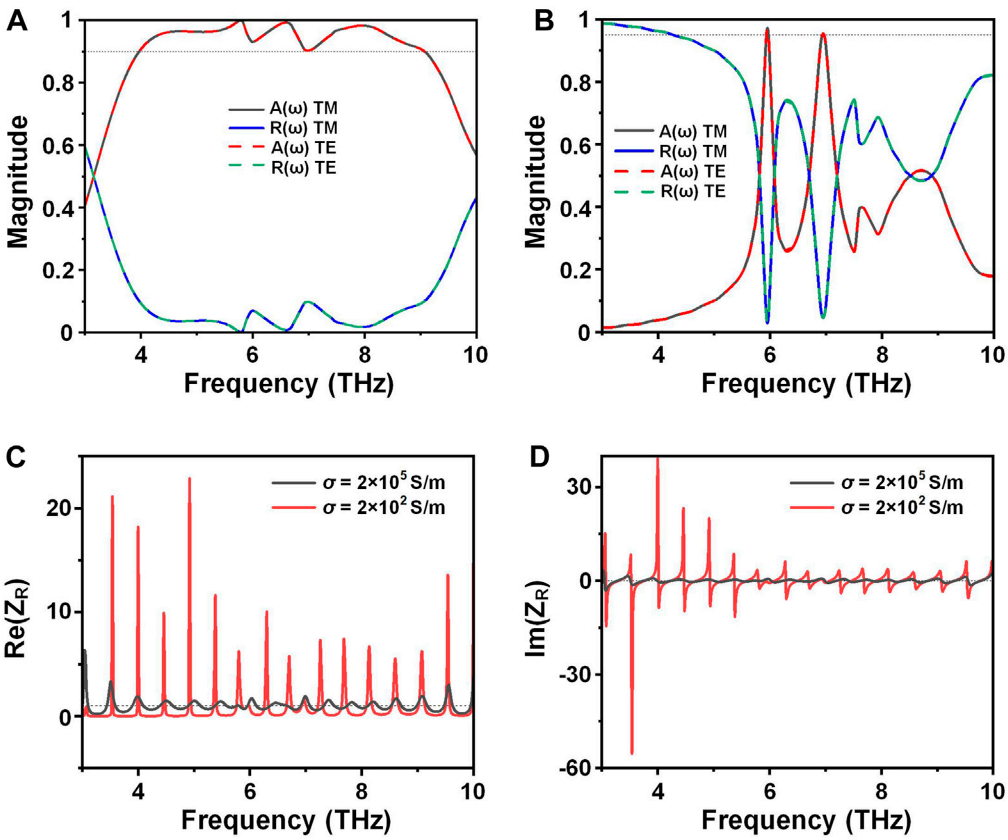

FIGURE 3
Reflection and absorption spectrums of the TMA at **(A)** high temperature (358 K) and **(B)** low temperature (298 K). **(C)** Real and **(D)** imaginary parts of the relative impedance between the TMA and the free space with VO_2 conductivity 2×10^5 S/m (black line) and 2×10^2 S/m (red line).

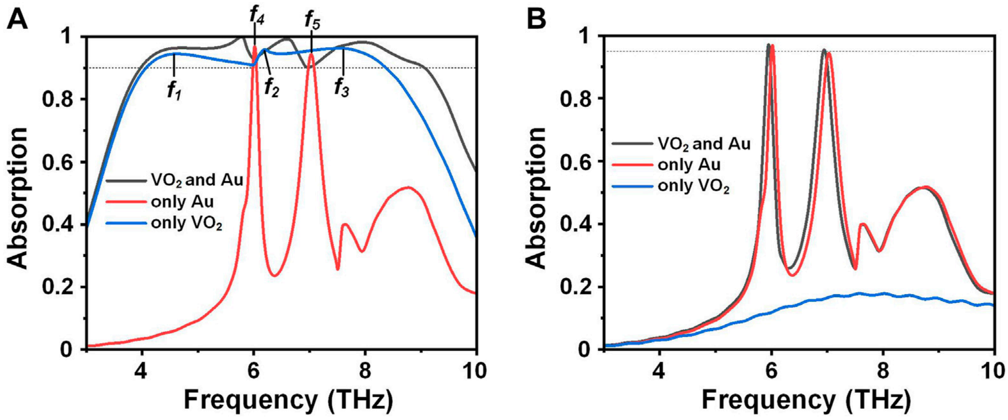

FIGURE 4
THz absorption spectra for TMA resonator array composed of hybrid VO_2 and Au resonators (black line), only Au resonators (red line) and only VO_2 resonators (blue line) at **(A)** high temperature (358 K) and **(B)** low temperature (298 K).

performance is greatly improved. Meanwhile, the TMA has the advantages of simple structure, polarization-independence and wide-angle absorption. The proposed TMA design scheme is expected to expand THz devices and enable a variety of applications in the THz range, such as modulation, sensing, stealth, and switching devices.

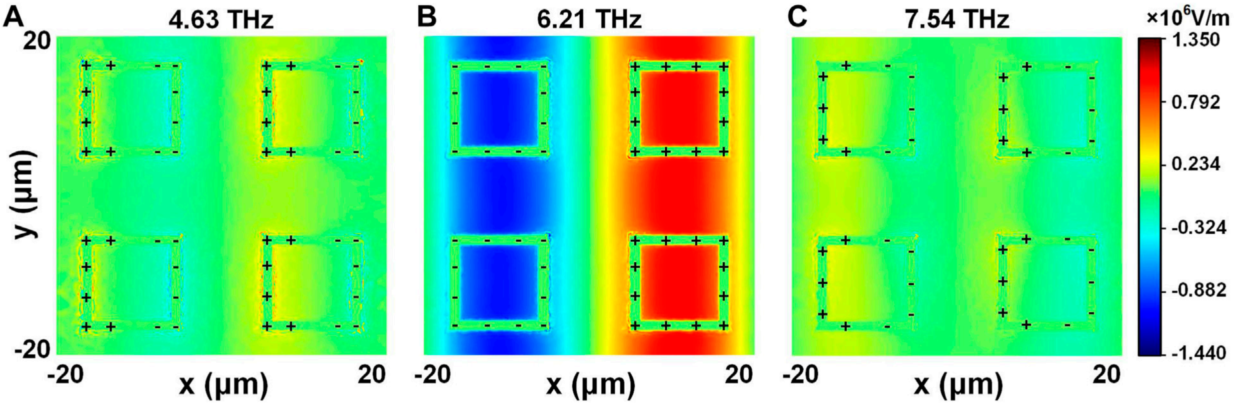

FIGURE 5
Electric field distributions (x-y plane) at the three absorption peaks in the presence of only VO_2 resonators in TMA. The peak frequencies are **(A)** f_1 = 4.63 THz **(B)** f_2 = 6.21 THz **(C)** f_3 = 7.54 THz, respectively.

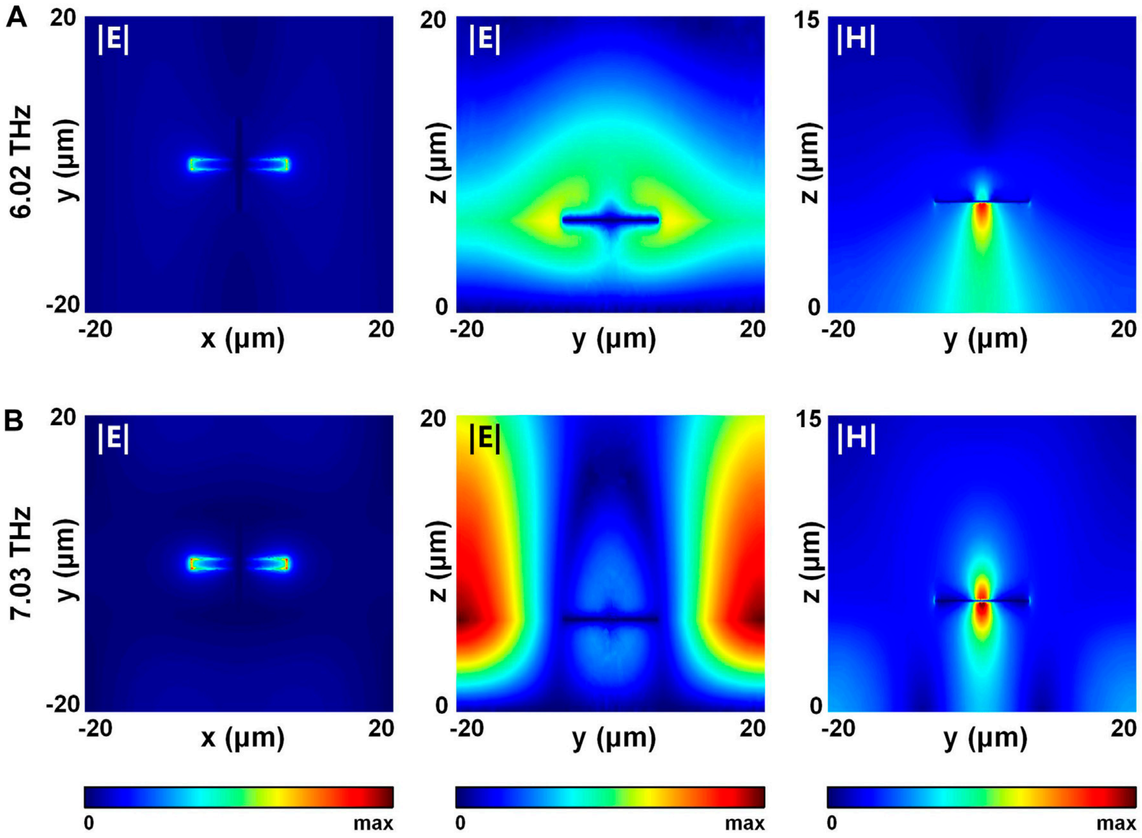

FIGURE 6
Electric field distributions and magnetic field distributions at the two resonant peaks in the presence of only Au resonators in TMA. The resonant peak frequencies are **(A)** f_4 = 6.02 THz (top row) **(B)** f_5 = 7.03 THz (bottom row), respectively. Left: electric field distributions (x-y plane), middle: electric field distributions (y-z plane), and right: magnetic field distributions (y-z plane).

2 Design and methods

The unit cell structure of the designed switchable TMA is shown in Figure 1. It consists of a resonator array above an Au conductive ground layer separated with a polyimide (PI) dielectric spacer, which includes four square-loop VO_2 resonators and a crossed Au resonator. As shown in Figure 1A, the period of the unit cell structure is P. The thickness of the resonators is t_1 for the Au

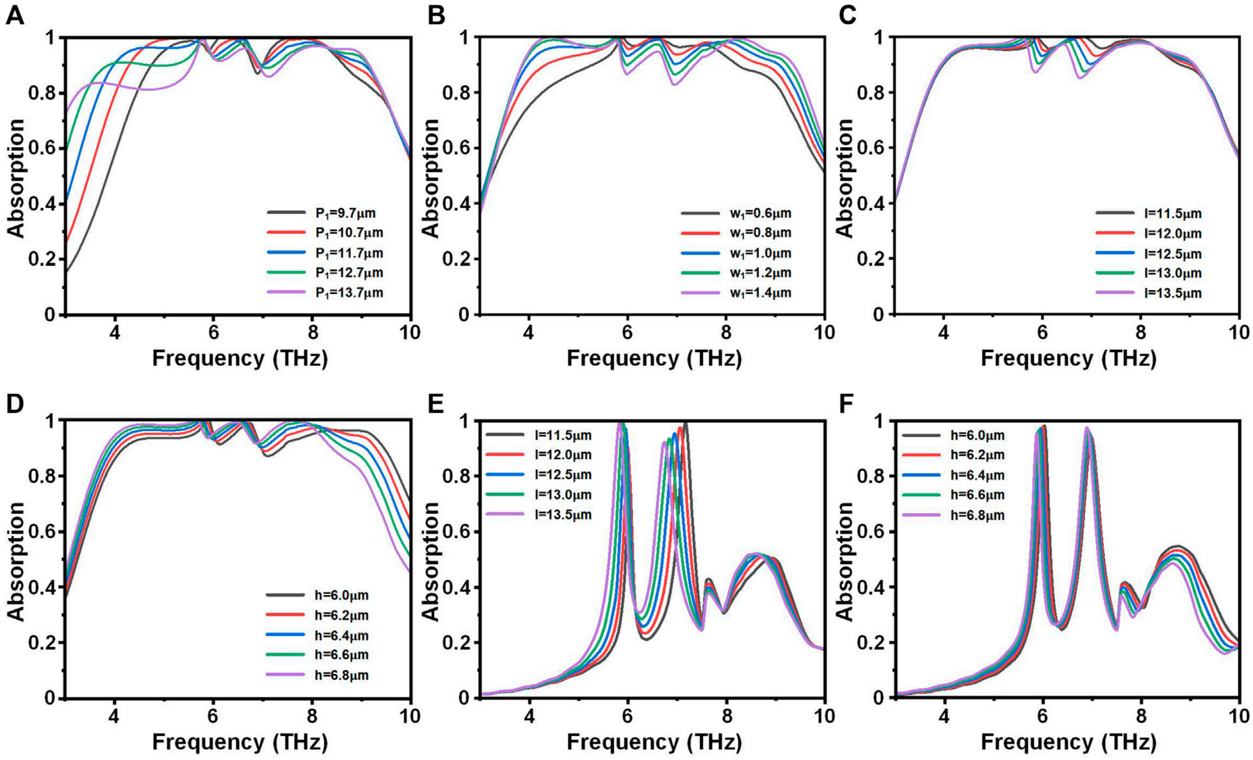

FIGURE 7
Dependency of structural parameters. Among them, **(A–D)** are at the temperature of T = 358 K, and **(E)** and **(F)** are at the temperature of T = 298 K.

resonator and t_2 for the four VO_2 resonators, respectively, and the thickness of the PI spacer is h. For the Au resonator, the length of the cross is l and the width is w, located in the middle of the resonator layer of each unit cell as shown in Figure 1B. Around it are four square-loop VO_2 resonators. Their side length is P_1, and the width of each side is w_1. The spacing between the VO_2 resonators in both x- and y-directions is d. The detailed structural parameters are set as: $p = 40\ \mu m$, $t_1 = 0.1\ \mu m$, $t_2 = 0.2\ \mu m$, $h = 6.4\ \mu m$, $l = 12.5\ \mu m$, $w = 1.1\ \mu m$, $P_1 = 11.7\ \mu m$, $w_1 = 1\ \mu m$, and $d = 10.1\ \mu m$.

The electromagnetic response of the designed TMA is simulated by the finite element method (FEM). Periodic boundary conditions are applied in both x- and y-directions, and two perfectly matching layers are used in the z-direction to eliminate spurious reflections caused by any impedance mismatch at the two boundaries. In the simulation, the relative permittivity of PI is 3 with the loss angle tangent $\delta = 0.03$ [59]. Due to the inherent loss of materials, it is helpful to improve the absorption performance of the designed TMA [60]. The relative permittivity of Au in the THz range can be described by the Drude dispersion model [61],

$$\varepsilon_{\mathrm{Au}} = 1 - \frac{\omega_p^{\ 2}}{\left(\omega^2 + i\gamma_{\mathrm{Au}}\omega\right)} \tag{1}$$

where the plasma frequency $\omega_p = 1.37 \times 10^{16}$ rad/s, and the collision frequency $\gamma_{\mathrm{Au}} = 4.05 \times 10^{13}$ rad/s [61]. Similarly, the dielectric dispersion of VO_2 in the THz range can also be expressed by the Drude model but with Lorentz correction [46],

$$\varepsilon_{\mathrm{VO_2}} = \varepsilon_\infty - \frac{\omega_p^{\ 2}(\sigma)}{\left(\omega^2 + i\gamma_{\mathrm{VO_2}}\omega\right)} \tag{2}$$

where $\varepsilon_\infty = 12$ is the high-frequency contribution to the relative permittivity, and the collision frequency $\gamma_{\mathrm{VO_2}} = 5.75 \times 10^{13}$ rad/s [46]. The plasma frequency of VO_2 is related to its conductivity σ, which can be expressed as [46],

$$\omega_p^{\ 2}(\sigma) = \frac{\sigma}{\sigma_0}\omega_p^{\ 2}(\sigma_0) \tag{3}$$

where the fitted parameters $\sigma_0 = 3 \times 10^5$ S/m and $\omega_p(\sigma_0) = 1.4 \times 10^{15}$ rad/s can match the dispersion measured in the experiment [46]. There is a thermal hysteresis line for the change in conductivity of VO_2, as shown in Figure 2. The conductivity of VO_2 can change rapidly with temperature heating or cooling, regardless of the speed of environmental temperature changes with negligible commutation time [62]. When the temperature rises from 298 K to 358 K, the conductivity increases from 2×10^2 S/m to 2×10^5 S/m, corresponding to its phase transition from a complete insulator state to a fully metallic state [50, 51]. The phase transition is reversible. The opposite transition occurs when the temperature decreases, corresponding to a variation in conductivity between 2×10^5 S/m (358 K) to 2×10^2 S/m (298 K).

The absorbance $A(\omega)$, reflectance $R(\omega)$ and transmittance $T(\omega)$ can be calculated by the S-parameters obtained from the frequency domain solver in the FEM. The absorption equation can be expressed as,

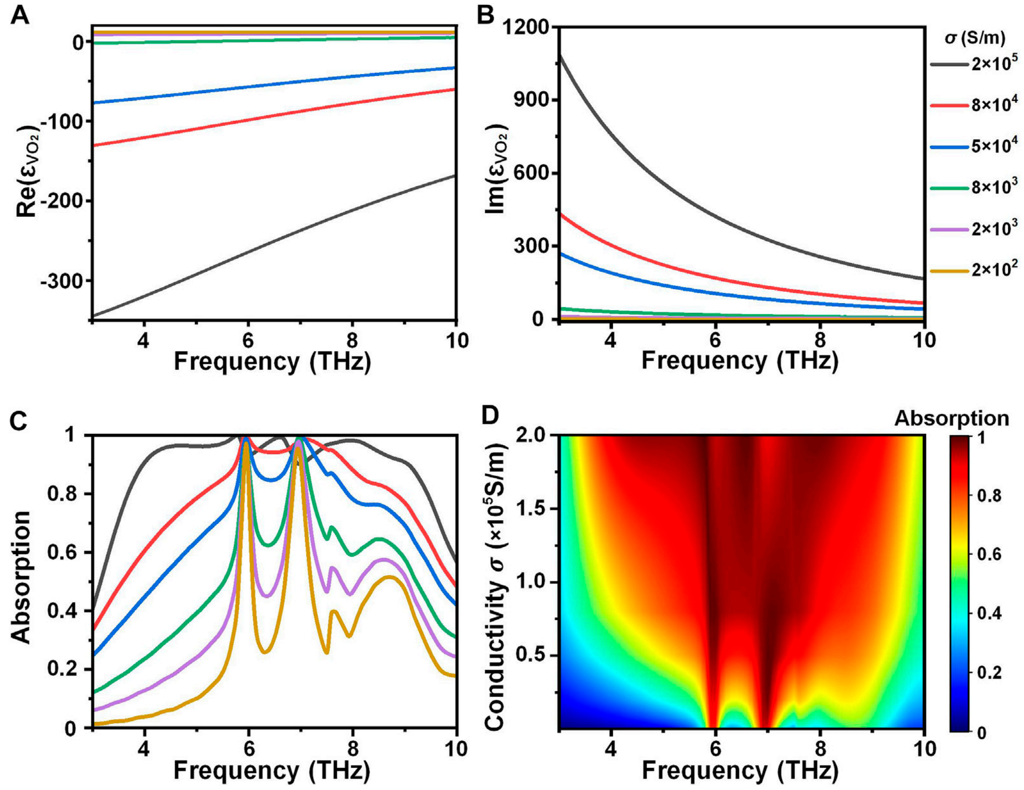

FIGURE 8
(A) Real and **(B)** imaginary parts of the relative permittivity of VO_2 under different conductivities. **(C)** Absorption performance of TMA under different conductivities. **(D)** Absorption performance as a function of the operating frequency and conductivity of VO_2.

$$A(\omega) = 1 - R(\omega) - T(\omega) = 1 - |S_{11}(\omega)|^2 - |S_{21}(\omega)|^2 \tag{4}$$

where $S_{11}\omega)$ represents the reflectivity, and $S_{21}\omega)$ represents the transmissivity. In the simulation, the thickness of the conductive ground layer is greater than the skin depth of THz wave, resulting in a transmissivity of approximately 0. Thus, the absorbance $A(\omega)$ can be simplified as,

$$A(\omega) = 1 - |S_{11}(\omega)|^2 \tag{5}$$

3 Results and discussion

The simulated absorption and reflection spectra of the designed TMA are shown in Figure 3. When in a high-temperature state (358 K), VO_2 is in a completely metallic phase. At this time, the THz spectral response of the proposed TMA under normal incidence is shown in Figure 3A. The TMA has an absorption rate of more than 90% in the ultra-broadband range of 3.98 to 9.06 THz, with a bandwidth exceeding 5 THz. The THz spectral response of TMA under normal incidence at a temperature of 298 K (VO_2 is in a complete insulator state) is shown in Figure 3B. The THz spectral response exhibits a dual-band high absorption with the absorption rates of 97.2% at 5.95 THz and 95.4% at 6.95 THz. With the phase transition of VO_2, the TMA achieves the switching between ultra-broadband absorption and dual-band absorption. Moreover, the metaatom resonators in one unit cell are arranged in a two-dimensional symmetry, thus eliminating the polarization dependence of TMA on the incident THz wave. The results in Figures 3A, B can also confirm this point with TM polarization and TE polarization incident separately.

The efficient absorption of TMA can be elucidated by the wave-interference theory and impedance matching theory. Obviously, in the absence of transmission, by minimizing the reflected waves through destructive interference, the absorption of TMA can be maximized. At this time, the effective permittivity and permeability of TMA can provide equivalent impedance to match the effective impedance in free space [63]. The relationship between absorption and relative impedance satisfies,

$$A(\omega) = 1 - R(\omega) = 1 - \left|\frac{Z - Z_0}{Z + Z_0}\right| = 1 - \left|\frac{Z_R - 1}{Z_R + 1}\right| \tag{6}$$

$$Z_R = \pm\sqrt{\frac{(1 + S_{11}(\omega))^2 - {S_{21}}^2(\omega)}{(1 - S_{11}(\omega))^2 - {S_{21}}^2(\omega)}} \tag{7}$$

where Z and Z_0 are the effective impedances of the TMA and the free space, respectively, and Z_R is the relative impedance between the TMA and the free space. When the impedances reach a perfect matching state, the real and imaginary parts of the relative

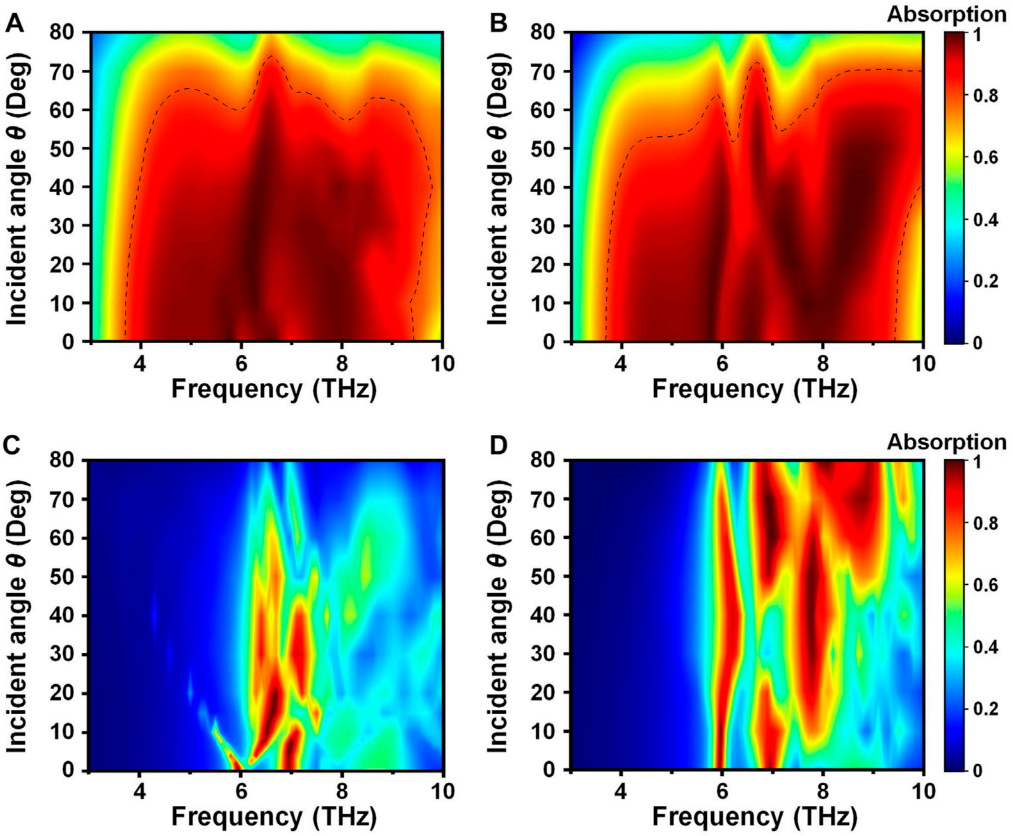

FIGURE 9
Broadband absorption spectra of TMA (at the temperature of 358 K) as a function of the operating frequency and incidence angle under the incidence with **(A)** TM and **(B)** TE polarization states, and dual-band absorption spectra of TMA (at the temperature of 298 K) as a function of the operating frequency and incidence angle under the incidence with **(C)** TM and **(D)** TE polarization states, respectively.

impedance can be attained to 1 and 0. The calculated relative impedance results when the VO_2 at 358 K ($\sigma = 2 \times 10^5$ S/m) and 298 K ($\sigma = 2 \times 10^2$ S/m) are shown in Figures 3C, D, respectively. When the real and imaginary parts of the relative impedance are around 1 and 0, respectively, the efficient absorption can be achieved, which corresponds to the state of impedance matching.

The absorption characteristics of our designed TMA are the combination of the absorption characteristics of Au and VO_2 resonators when they exist independently. These VO_2 resonators have different absorption characteristics at different temperatures, thus providing operability for the switching between broadband and dual-band absorption of our designed TMA. At the temperature where VO_2 is in a completely metallic phase, the absorption performance of a metamaterial absorber composed solely of Au or VO_2 resonators is shown in Figure 4A. It can be seen that the only VO_2 resonators provide a broadband absorption from 4.07 to 8.37 THz with three absorption peaks at $f_1 = 4.63$ THz, $f_2 = 6.21$ THz and $f_3 = 7.54$ THz, and a dual-band absorption is formed at $f_4 = 6.02$ THz and $f_5 = 7.03$ THz with only Au resonators. At the temperature where VO_2 is in a complete insulator phase, it can be seen from Figure 4B that the absorption drops sharply with only VO_2 resonators compared to the high temperature condition. But under this low temperature state, the absorption of the absorber composed of Au resonators remains unchanged. The absorption characteristics of our designed TMA is determined by the absorption characteristics of only Au and only VO_2 resonators. Therefore, the absorption characteristics of the combination of Au and VO_2 resonators can be switched between broadband and dual-band with the help of temperature control.

The broadband absorption effect of our proposed TMA is mainly provided by the VO_2 resonators. To further explore the physical origin of the designed TMA, the electric field distributions at the three absorption peaks in the presence of only VO_2 resonators are presented in Figure 5. Since our proposed TMA is polarization-independent, here, the electric field distributions are presented only under TM polarization incidence. It can be seen that the electric field distributions at $f_1 = 4.63$ THz and $f_3 = 7.54$ THz are similar with the positive charges concentrated on the left side of the square-loop and the negative charges concentrated on the right side. This indicates that both absorption peaks are caused by the excitation of electric dipole resonance, but the difference is that the intensity of charge accumulation is different. As for $f_2 = 6.21$ THz, in a unit cell with four square-loops, negative charges are induced on the two loops on the left, while positive charges are induced on the right. This suggests a dipole resonance that occurs between two adjacent loops in the horizontal direction. The local electric field intensity can reach 10^6 V/m level, which can be explained by the coupled mode theory [64]. Therefore, electrical dipole resonances are responsible for all three absorption peaks and expand into broadband in the presence of only VO_2 resonators.

In the presence of only Au resonators, the electric field distributions and magnetic field distributions at the two resonant peaks are shown in Figure 6. From the electric field distributions in the x-y plane, it can be seen that the electric field distributions at the two frequencies f_4 = 6.02 THz and f_5 = 7.03 THz are similar. However, combining the distributions of electric and magnetic fields in the y-z plane, it can be seen that there are significant differences between the two resonance modes. In these two resonances, the f_4 mode is a dark surface-Bloch mode related to the periodic constant [65]. If the period of the unit cell structure decreases to a certain value, the dark surface-Bloch mode resonance will disappear. In contrast, the electrical dipole resonance at the f_5 mode does not disappear with the decrease of the period. Thus, the dual-band absorption originates the electrical dipole mode and nonlocal surface-Bloch mode of metal resonators at low temperature (298 K).

The dependency of structural parameters is shown in Figure 7. Based on the designed parameters, each subgraph is obtained by ensuring that only one parameter is a variable. Among them, Figures 7A–D show the results obtained at the temperature of 358 K, while Figures 7E, F show the results obtained at 298 K. The simulation results show that the geometric parameters have a non-negligible influence on the absorption performance. Because our proposed TMA can be switch between ultra-broadband and dual-band, it is necessary to consider the influence of different parameters on the absorption rate at both low and high temperatures. Thus, the designed parameters are the optimized parameters obtained from our comprehensive consideration at both low and high temperature conditions.

The conductivity of VO_2 can vary with the temperature with a thermal hysteresis loop [62]. The change in conductivity caused by different temperatures leads to a change in the permittivity dispersion of VO_2. The real and imaginary parts of the relative permittivity under different conductivities are shown in Figures 8A, B. Thus, our designed TMA has the performance of continuously adjustable absorption efficiency with temperature. The absorption performance of TMA under different conductivities is shown in Figure 8C, and the absorption performance under continuous conductivity changes is presented in Figure 8D. It can be clearly seen that as the conductivity changes, the absorption performance transitions between dual-band absorption and ultra-broadband absorption.

Additionally, the broadband absorption spectra of TMA (at the temperature of 358 K) as a function of the operating frequency and incidence angle are discussed, under the incidence with TM and TE polarization states, respectively, as shown in Figures 9A, B, and the dual-band absorption spectra of TMA (at the temperature of 298 K) as a function of the operating frequency and incidence angle are shown in Figures 9C, D under the incidence with TM and TE polarization states, respectively. In Figures 9A, B, the red-highlighted area (within the black dashed line) indicates the broadband of angle-dependent absorption efficiency exceeding 80% level. It can be seen that the proposed TMA can work over a wide range of incident angles under both incidence cases with TM polarization state and TE polarization state. The frequency range of broadband absorption is basically unchanged. The effective working angles for broadband absorption with more than 80% absorption efficiency under oblique incidence can reach up to nearly 60° for TM polarization, and 50° for TE polarization. Due to the impedance mismatch and higher order scattering, the TMA broadband absorption tends to be deteriorated at a wider oblique incidence angle. In stark contrast, the dual-band absorption at 298 K is greatly affected by the incidence angle especially under TM polarization state, as shown in Figures 9C, D. However, in any case, there is a certain angle to meet the working conditions, which reduces the requirement for system alignment.

4 Conclusion

In conclusion, we have realized a TMA that can be switched flexibly between ultra-broadband and dual bands by changing the conductivity of VO_2 through thermal control. The TMA comprises a resonator array above a conductive ground layer separated with a dielectric spacer, which includes four square-loop VO_2 resonators and a crossed Au resonator in each unit cell. The TMA can achieve more than 90% absorption bandwidth in the range of 3.98 to 9.06 THz at high temperature (VO_2 is in the completely metallic state), which can be elucidated by the wave-interference theory and impedance matching theory. At low temperature where VO_2 is fully insulated, the TMA realizes a dual-band absorption with the absorption efficiency exceeding 95% at 5.95 and 6.95 THz, which originates the dipole mode and nonlocal surface-Bloch mode of metal resonators. The TMA has the advantage of polarization-independence, due to the two-dimensional symmetry of structural arrangement. In addition, the broadband absorbance can remain more than 80% over a wide range of incident angles, specifically up to nearly 60° for TM polarization, and 50° for TE polarization. Compared with previous studies, our design can switch between two absorption modes and its absorption performance is greatly improved. The proposed TMA design scheme is expected to expand THz devices and has many potential applications in the THz range, such as modulation, sensing, stealth, and switching devices.

Data availability statement

The original contributions presented in the study are included in the article/Supplementary Material, further inquiries can be directed to the corresponding author.

Author contributions

ZR, WW, and RW conceived and led the design. ZR, WW, SL, and RW finished the whole manuscript writing and manuscript modification. WW, YZ, SC, and GR performed the statistical analysis. WW and YZ performed image processing. ZR, WW, GR, SL, and RW contributed to the proofreading and revised the article format. All authors contributed to the article and approved the submitted version.

Funding

This work was supported in part by the National Natural Science Foundation of China (62205106), Fundamental Research Funds for the Central Universities (2022MS122 and 2019MS118), Natural Science Foundation of Hebei Province (A2019502044) and Program for New Century Excellent Talents in University (NCET-12-0844).

Conflict of interest

The authors declare that the research was conducted in the absence of any commercial or financial relationships that could be construed as a potential conflict of interest.

Publisher's note

References

1. Sengupta K, Nagatsuma T, Mittleman DM. Terahertz integrated electronic and hybrid electronic–photonic systems. *Nat Elect* (2018) 1:622–35. doi:10.1038/s41928-018-0173-2

2. Zhang X, Xu Q, Xia L, Li Y, Gu J, Tian Z, et al. Terahertz surface plasmonic waves: A review. *Adv Photon* (2020) 2:014001. doi:10.1117/1.AP.2.1.014001

3. Wang Y, Han Z, Du Y, Qin J. Ultrasensitive terahertz sensing with high-q toroidal dipole resonance governed by bound states in the continuum in all-dielectric metasurface. *Nanophotonics* (2021) 10:1295–307. doi:10.1515/nanoph-2020-0582

4. Stantchev RI, Yu X, Blu T, Pickwell-MacPherson E. Real-time terahertz imaging with a single-pixel detector. *Nat Commun* (2020) 11:2535. doi:10.1038/s41467-020-16370-x

5. Yang Y, Yamagami Y, Yu X, Pitchappa P, Webber J, Zhang B, et al. Terahertz topological photonics for on-chip communication. *Nat Photon* (2020) 14:446–51. doi:10.1038/s41566-020-0618-9

6. Zhou Y, Qin Z, Liang Z, Meng D, Xu H, Smith DR, et al. Ultra-broadband metamaterial absorbers from long to very long infrared regime. *Light: Sci Appl* (2021) 10:138. doi:10.1038/s41377-021-00577-8

7. Yu H, Meng D, Liang Z, Xu H, Qin Z, Su X, et al. Polarization-dependent broadband absorber based on composite metamaterials in the long-wavelength infrared range. *Opt Express* (2021) 29:36111–20. doi:10.1364/OE.435579

8. Zhao Y, Askarpour AN, Sun L, Shi J, Li X, Alù A. Chirality detection of enantiomers using twisted optical metamaterials. *Nat Commun* (2017) 8:14180. doi:10.1038/ncomms14180

9. Xu Q, Su X, Zhang X, Dong L, Liu L, Shi Y, et al. Mechanically reprogrammable pancharatnam–berry metasurface for microwaves. *Adv Photon* (2022) 4:016002. doi:10.1117/1.AP.4.1.016002

10. Grady N, Heyes J, Chowdhury D, Zeng Y, Reiten M, Azad A, et al. Terahertz metamaterials for linear polarization conversion and anomalous refraction. *Science* (2013) 340:1304–7. doi:10.1126/science.1235399

11. Wang R, Ansari MA, Ahmed H, Li Y, Cai W, Liu Y, et al. Compact multi-foci metalens spectrometer. *Light: Sci Appl* (2023) 12:103. doi:10.1038/s41377-023-01148-9

12. Wang R, Ren G, Ren Z, Liu J, Li S, Chen X, et al. Reconstructing subwavelength resolution terahertz holographic images. *Opt Express* (2022) 30:7137–46. doi:10.1364/OE.453634

13. Wang R, Intaravanne Y, Li S, Han J, Chen S, Liu J, et al. Metalens for generating a customized vectorial focal curve. *Nano Lett* (2021) 21:2081–7. doi:10.1021/acs.nanolett.0c04775

14. Fu X, Cui T. Recent progress on metamaterials: From effective medium model to real-time information processing system. *Prog Quan Elect* (2019) 67:100223. doi:10.1016/j.pquantelec.2019.05.001

15. Pitchappa P, Kumar A, Singh R, Wang N. Electromechanically tunable frequency-agile metamaterial bandpass filters for terahertz waves. *Adv Opt Mater* (2022) 10:2101544. doi:10.1002/adom.202101544

16. Jung H, Jo H, Lee W, Kang MS, Lee H. Reconfigurable molecularization of terahertz meta-atoms. *ACS Photon* (2022) 9:1814–20. doi:10.1021/acsphotonics.2c00397

17. Zhao X, Wang Y, Schalch J, Duan G, Cremin K, Zhang J, et al. Optically modulated ultra-broadband all-silicon metamaterial terahertz absorbers. *ACS Photon* (2019) 6:830–7. doi:10.1021/acsphotonics.8b01644

18. Islam M, Sultana J, Biabanifard M, Vafapour Z, Nine M, Dinovitser A, et al. Tunable localized surface plasmon graphene metasurface for multiband superabsorption and terahertz sensing. *Carbon* (2020) 158:559–67. doi:10.1016/j.carbon.2019.11.026

19. Yu P, Yang H, Chen X, Yi Z, Yao W, Chen J, et al. Ultra-wideband solar absorber based on refractory titanium metal. *Renew Energ* (2020) 158:227–35. doi:10.1016/j.renene.2020.05.142

20. Wang R, Han J, Liu J, Tian H, Sun W, Li L, et al. Multi-foci metalens for terahertz polarization detection. *Opt Lett* (2020) 45:3506–9. doi:10.1364/OL.395580

21. Song Z, Zhang J. Achieving broadband absorption and polarization conversion with a vanadium dioxide metasurface in the same terahertz frequencies. *Opt Express* (2020) 28:12487–97. doi:10.1364/OE.391066

22. Ren Z, Chang S, Li S, Wang R. Birefringent dielectric multi-foci metalens for polarization detection. *Physica Scripta* (2023) 98:045502. doi:10.1088/1402-4896/acbe35

23. Sun K, Zhao Z, Cai Y, Levy U, Han Z. Ultra-narrowband and highly-directional thz thermal emitters based on the bound state in the continuum. *Nanophotonics* (2021) 10:4035–43. doi:10.1515/nanoph-2021-0380

24. Zheng Z, Luo Y, Yang H, Yi Z, Zhang J, Song Q, et al. Thermal tuning of terahertz metamaterial absorber properties based on VO_2. *Phys Chem Chem Phys* (2022) 24:8846–53. doi:10.1039/d2cp01070d

25. Torkaman P, Darbari S, Mohammad-Zamani M. Design and simulation of a piezotronic gan-based pulsed thz emitter. *J Lightwave Tech* (2018) 36:3645–51. doi:10.1109/JLT.2018.2844219

26. Chai M, Wang Y, Chen C, Zhao Z, Jin M, He T. Metamaterials-based photoelectric conversion: From microwave to optical range. *Laser Photon Rev* (2022) 16:2100458. doi:10.1002/lpor.202100458

27. Huang Y, Kaj K, Chen C, Yang Z, Ul Haque SR, Zhang Y, et al. Broadband terahertz silicon membrane metasurface absorber. *ACS Photon* (2022) 9:1150–6. doi:10.1021/acsphotonics.2c00166

28. Obaidullah M, Esat V, Sabah C. Multi-band (9, 4) chiral single-walled carbon nanotube based metamaterial absorber for solar cells. *Opt Laser Tech* (2021) 134:106623. doi:10.1016/j.optlastec.2020.106623

29. Chen H, Ma W, Huang Z, Zhang Y, Huang Y, Chen Y. Graphene-based materials toward microwave and terahertz absorbing stealth technologies. *Adv Opt Mater* (2019) 7:1801318. doi:10.1002/adom.201801318

30. Shui W, Li J, Wang H, Xing Y, Li Y, Yang Q, et al. $Ti_3C_2T_x$ MXene sponge composite as broadband terahertz absorber. *Adv Opt Mater* (2020) 8:2001120. doi:10.1002/adom.202001120

31. Geng M, Liu Z, Chen H, Bao X, Yang X, Lu W. Flexible and dual-tunable radar absorber enabled by graphene. *Adv Mater Tech* (2022) 7:2200028. doi:10.1002/admt.202200028

32. Tao H, Landy NI, Bingham CM, Zhang X, Averitt RD, Padilla WJ. A metamaterial absorber for the terahertz regime: Design, fabrication and characterization. *Opt Express* (2008) 16:7181–8. doi:10.1364/OE.16.007181

33. Huang X, He W, Yang F, Ran J, Gao B, Zhang WL. Polarization-independent and angle-insensitive broadband absorber with a target-patterned graphene layer in the terahertz regime. *Opt Express* (2018) 26:25558–66. doi:10.1364/OE.26.025558

34. Wu X, Zheng Y, Luo Y, Zhang J, Yi Z, Wu X, et al. A four-band and polarization-independent bds-based tunable absorber with high refractive index sensitivity. *Phys Chem Chem Phys* (2021) 23:26864–73. doi:10.1039/d1cp04568g

35. Wang B, Tang C, Niu Q, He Y, Chen T. Design of narrow discrete distances of dual-/triple-band terahertz metamaterial absorbers. *Nanoscale Res Lett* (2019) 14:1–7. doi:10.1186/s11671-019-2876-3

36. Li Y, Gao W, Guo L, Chen Z, Li C, Zhang H, et al. Tunable ultra-broadband terahertz perfect absorber based on vanadium oxide metamaterial. *Opt Express* (2021) 29:41222–33. doi:10.1364/OE.444761

37. Ding Z, Su W, Lu H, Wu H, Yao H. Terahertz absorber based on double-layer graphene metasurface with tunable absorption window and intensity. *Opt Laser Tech* (2023) 163:109446. doi:10.1016/j.optlastec.2023.109446

38. Wang D, Xu KD, Luo S, Cui Y, Zhang L, Cui J. A high q-factor dual-band terahertz metamaterial absorber and its sensing characteristics. *Nanoscale* (2023) 15:3398–407. doi:10.1039/d2nr05820k

39. Wang R, Li L, Liu J, Yan F, Tian F, Tian H, et al. Triple-band tunable perfect terahertz metamaterial absorber with liquid crystal. *Opt Express* (2017) 25:32280–9. doi:10.1364/OE.25.032280

40. Zhang H, Wang Z, Hu C, Liu H. A tailored broadband terahertz metamaterial absorber based on the thermal expansion feature of liquid metal. *Results Phys* (2020) 16: 102937. doi:10.1016/j.rinp.2020.102937

41. Lari ES, Vafapour Z, Ghahraloud H. Optically tunable triple-band perfect absorber for nonlinear optical liquids sensing. *IEEE Sensors J* (2020) 20:10130–7. doi:10.1109/JSEN.2020.2989742

42. Gong Y, Hu F, Jiang M, Zhang L, Zou Y, Jiang G, et al. Terahertz binary coder based on graphene metasurface. *Carbon* (2021) 184:167–76. doi:10.1364/OE.390835

43. Zhang M, Song Z. Switchable terahertz metamaterial absorber with broadband absorption and multiband absorption. *Opt Express* (2021) 29:21551–61. doi:10.1364/OE.432967

44. Qi L, Liu C, Shah SMA. A broad dual-band switchable graphene-based terahertz metamaterial absorber. *Carbon* (2019) 153:179–88. doi:10.1016/j.carbon.2019.07.011

45. Liu M, Hwang HY, Tao H, Strikwerda AC, Fan K, Keiser GR, et al. Terahertz-field-induced insulator-to-metal transition in vanadium dioxide metamaterial. *Nature* (2012) 487:345–8. doi:10.1038/nature11231

46. Huang J, Li J, Yang Y, Li J, Li J, Zhang Y, et al. Broadband terahertz absorber with a flexible, reconfigurable performance based on hybrid-patterned vanadium dioxide metasurfaces. *Opt Express* (2020) 28:17832–40. doi:10.1364/OE.394359

47. Wuttig M, Bhaskaran H, Taubner T. Phase-change materials for non-volatile photonic applications. *Nat Photon* (2017) 11:465–76. doi:10.1038/nphoton.2017.126

48. Kübler C, Ehrke H, Huber R, Lopez R, Halabica A, Haglund R, Jr, et al. Coherent structural dynamics and electronic correlations during an ultrafast insulator-to-metal phase transition in VO_2. *Phys Rev Lett* (2007) 99:116401. doi:10.1103/PhysRevLett.99.116401

49. Ko B, Badloe T, Rho J. Vanadium dioxide for dynamically tunable photonics. *ChemNanoMat* (2021) 7:713–27. doi:10.1002/cnma.202100060

50. Qazilbash MM, Brehm M, Chae BG, Ho PC, Andreev GO, Kim BJ, et al. Mott transition in VO_2 revealed by infrared spectroscopy and nano-imaging. *Science* (2007) 318:1750–3. doi:10.1126/science.1150124

51. Chen L, Song Z. Simultaneous realizations of absorber and transparent conducting metal in a single metamaterial. *Opt Express* (2020) 28:6565–71. doi:10.1364/OE.388066

52. Liu H, Wang ZH, Li L, Fan YX, Tao ZY. Vanadium dioxide-assisted broadband tunable terahertz metamaterial absorber. *Scientific Rep* (2019) 9:5751. doi:10.1038/s41598-019-42293-9

53. Jiao XF, Zhang ZH, Li T, Xu Y, Song GF. Tunable dual broadband terahertz metamaterial absorber based on vanadium dioxide. *Appl Sci* (2020) 10:7259. doi:10.3390/app10207259

54. Huang J, Li J, Yang Y, Li J, Zhang Y, Yao J, et al. Active controllable dual broadband terahertz absorber based on hybrid metamaterials with vanadium dioxide. *Opt Express* (2020) 28:7018–27. doi:10.1364/OE.387156

55. Zheng Z, Zheng Y, Luo Y, Yi Z, Zhang J, Liu Z, et al. A switchable terahertz device combining ultra-wideband absorption and ultra-wideband complete reflection. *Phys Chem Chem Phys* (2022) 24:2527–33. doi:10.1039/d1cp04974g

56. Liu W, Xu J, Song Z. Bifunctional terahertz modulator for beam steering and broadband absorption based on a hybrid structure of graphene and vanadium dioxide. *Opt Express* (2021) 29:23331–40. doi:10.1364/OE.433364

57. Qiu Y, Yan DX, Feng QY, Li XJ, Zhang L, Qiu GH, et al. Vanadium dioxide-assisted switchable multifunctional metamaterial structure. *Opt Express* (2022) 30: 26544–56. doi:10.1364/OE.465062

58. Wang D, Sun S, Feng Z, Tan W. Enabling switchable and multifunctional terahertz metasurfaces with phase-change material. *Opt Mater Express* (2020) 10:2054–65. doi:10.1364/OME.397173

59. Liu S, Chen H, Cui TJ. A broadband terahertz absorber using multi-layer stacked bars. *Appl Phys Lett* (2015) 106:151601. doi:10.1063/1.4918289

60. Cunningham PD, Valdes NN, Vallejo FA, Hayden LM, Polishak B, Zhou XH, et al. Broadband terahertz characterization of the refractive index and absorption of some important polymeric and organic electro-optic materials. *J Appl Phys* (2011) 109: 043505. doi:10.1063/1.3549120

61. Ordal MA, Bell RJ, Alexander RW, Long LL, Querry MR. Optical properties of fourteen metals in the infrared and far infrared: Al, Co, Cu, Au, Fe, Pb, Mo, Ni, Pd, Pt, Ag, Ti, V, and W. *Appl Opt* (1985) 24:4493–9. doi:10.1364/ao.24.004493

62. Zheng Z, Zheng Y, Luo Y, Yi Z, Zhang J, Liu L, et al. Terahertz perfect absorber based on flexible active switching of ultra-broadband and ultra-narrowband. *Opt Express* (2021) 29:42787–99. doi:10.1364/OE.445155

63. Chen H. Interference theory of metamaterial perfect absorbers. *Opt Express* (2012) 20:7165–72. doi:10.1364/OE.20.007165

64. Yong Z, Zhang S, Gong C, He S. Narrow band perfect absorber for maximum localized magnetic and electric field enhancement and sensing applications. *Scientific Rep* (2016) 6:24063. doi:10.1038/srep24063

65. Wang J, Tian H, Wang Y, Li X, Cao Y, Li L, et al. Liquid crystal terahertz modulator with plasmon-induced transparency metamaterial. *Opt Express* (2018) 26: 5769–76. doi:10.1364/oe.26.005769